

PAPER

Enhanced Distal Radius Segmentation in DXA Using Modified ASM

Sihyoung LEE[†], Sunil CHO^{††}, *Nonmembers*, and Yong Man RO^{†a)}, *Member*

SUMMARY The active shape model (ASM) has been widely adopted by automated bone segmentation approaches for radiographic images. In radiographic images of the distal radius, multiple edges are often observed in the near vicinity of the bone, typically caused by the presence of thin soft tissue. The presence of multiple edges decreases the segmentation accuracy when segmenting the distal radius using ASM. In this paper, we propose an enhanced distal radius segmentation method that makes use of a modified version of ASM, reducing the number of segmentation errors. To mitigate segmentation errors, the proposed method emphasizes the presence of the bone edge and downplays the presence of a soft tissue edge by making use of Dual energy X-ray absorptiometry (DXA). To verify the effectiveness of the proposed segmentation method, experiments were performed with 30 distal radius patient images. For the images used, compared to ASM-based segmentation, the proposed method improves the segmentation accuracy with 47.4% (from 0.974 mm to 0.512 mm).

key words: active shape model, distal radius, osteoporosis, segmentation

1. Introduction

Osteoporosis is a systemic skeletal disease characterized by low bone mass and microarchitectural deterioration of bone tissue, with a consequent increase in bone fragility and susceptibility to fracture [1]. In particular, after their menopause, women are more likely to suffer from the disease than men [2]. Further, the lack of symptoms makes it hard for patients to recognize the disease themselves.

Bone mineral density (BMD) measurement is regarded as an essential criterion for evaluating a patient's risk of suffering from osteoporosis and having bone fracture. BMD can be measured at specific fracture-related skeletal sites by different quantitative techniques: single photon absorptiometry (SPA), dual photon absorptiometry (DPA), and Dual energy X-ray absorptiometry (DXA). DXA has become the de facto standard for diagnosing osteoporosis because of its precise and acceptably accurate measures of BMD [3], [4]. For this purpose, several clinically relevant sites are widely used: proximal femur, vertebrae, and distal radius. These are the three major fracture-related skeletal sites.

Automatic image segmentation is an essential technique for measuring BMD, and which segmentation method to apply is strongly dependent on the image type and the

image characteristics in use. Because a bone generally has a specific shape according to its type, segmentation based on the active shape model (ASM) has been widely accepted for extracting the shape of bones from digital radiographic images [5]. Given the statistical shape model of a bone computed from a set of labeled training images, ASM iteratively tries to fit the model to the contour of the bones in a set of test images.

Rebuffel *et al.* [5] proposed a method for modeling and segmenting contours with inconsistent loops and bifurcations. It was observed that segmentation errors occur because the number of loops and the position of the bifurcation points on an object may vary in a complex way. The method parameterized contours in terms of a primary contour's landmarks along with a suitably constrained warp to a secondary contour. A k-nearest neighbor (K-NN) method was adopted for matching the statistical model for an object to test images. Zamora *et al.* [6] proposed a fully automated method for segmenting vertebrae using ASM. A customized Generalized Hough Transform was used to estimate the pose of the vertebrae by matching a template that represents the vertebrae of interest to a target image. Sotoca *et al.* [7] presented a semi-automated segmentation method for hand bones using ASM. To determine the orientation angle for a test finger, the system had adopted a finger template. After providing the center information of the finger from the user, the template is oriented in different angles, and the average grey level inside the template is observed for each angle.

In general, ASM assumes that only one edge exists near the boundary of an object in a test image; it then tries to fit the statistical shape model to the object boundary by adjusting the model. If multiple edges are present around an object boundary, ASM has no alternative but to produce segmentation errors when fitting the model to the object boundary. Because soft tissue at the distal radius is thinner than at other major fracture sites like proximal femur and vertebrae [8], multiple edges can typically be observed in the near vicinity of distal radius on digital radiograph images [9]. Accordingly, the segmentation error for distal radius is higher than for other major fracture sites. In this paper, we propose a new distal radius segmentation method using a modified version of ASM, mitigating segmentation errors caused by the presence of multiple edges. The proposed method emphasizes the presence of bone edges and downplays the presence of soft tissue edges by taking into account decomposed DXA images of bones.

Manuscript received July 13, 2010.

Manuscript revised November 2, 2010.

[†]The authors are with the Image and Video Systems Lab, Department of Electrical Engineering, KAIST, 335 Gwahak-ro, Yuseong-gu, Daejeon 305-732, Republic of Korea.

^{††}The author is with the Agency for Defense Development of the Republic of Korea.

a) E-mail: ymro@ee.kaist.ac.kr

DOI: 10.1587/transinf.E94.D.363

The paper is organized as follows. The limitation of distal radius segmentation with conventional ASM is described in Sect. 2, and the proposed segmentation method for distal radius is outlined in Sect. 3. Section 4 discusses our performance evaluation, comparing the proposed segmentation method with ASM-based segmentation. Conclusions are provided in Sect. 5.

2. Distal Radius ASM Segmentation Errors

ASM tries to find the optimum location of the contour of an object by iteratively matching a statistical shape model to a test image. The statistical shape model is constructed by means of a point distribution model (PDM) [10]. PDM models the statistical distribution of the shape of an object present in a set of training images. These training images are manually annotated with a set of points (called landmarks), along with the boundary of the object (see Sect. 3.1). ASM starts by placing the mean shape of an object, modeled using PDM, on a test image. This test image is then sampled at each landmark. For each sampled point, referred to as a model point in the test image, the best matching point along the normal to the model boundary is determined, resulting in an update of the model parameters. The best matching point is estimated by comparing the Mahalanobis distance between two profiles representing edge distribution at the model point and the corresponding landmark (see Sect. 3.3 for profiles).

Each iteration moves the model point to a new point that minimizes the Mahalanobis distance. This iterative process can be considered as a process that moves the model point to the object edge. The magnitude of the displacements is proportional to the strength of the object edge [11], based on the assumption that only one edge is present around the sample point.

In the iterative process, if multiple edges are present near the model point, the displacement of the model point can be non-intended, thus producing segmentation errors. Figure 1 shows two kinds of edges around the model point in digital radiographs: the bone edge (between the bone and the soft tissue) and the soft tissue edge (between the soft tissue and the air). Because of the presence of multiple edges, it is difficult to decide for ASM which edge is truly related to the object boundary.

In digital radiographic images of the distal radius, multiple edges are often observed in the near vicinity of the target object boundary because the thickness of soft tissue around the distal radius is thin. Observed segmentation errors are typically caused by the presence of multiple edges. Figure 2 shows the result achieved when using ASM for segmenting the distal radius. The region inside the box with solid line borders in the left figure is enlarged in the right figure. In the enlarged image, the ASM-based segmentation result is shown with a solid line, whereas the dashed line represents the true edge (manually annotated contour of the distal radius). The segmentation error can be clearly seen by comparing the dashed line with the solid line. The seg-

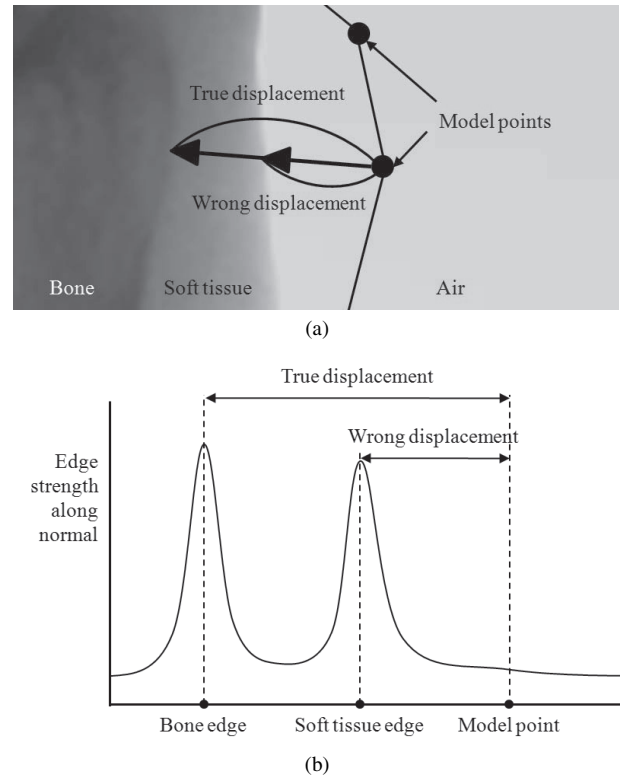


Fig. 1 Displacing the model point to the bone edge: (a) true vs. wrong displacement; (b) distribution of the edge strength around the model point.

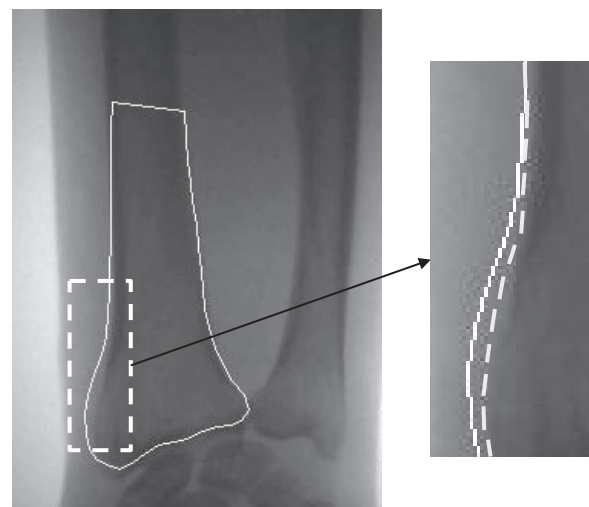


Fig. 2 Errors when segmenting distal radius using ASM.

mentation error results from the fact that the edge between the soft tissue and the background region is mistaken for the target edge.

3. Proposed Segmentation Method

An overview of the proposed segmentation method is shown in Fig. 3. The proposed distal radius segmentation method consists of three parts: training distal radius model, DXA

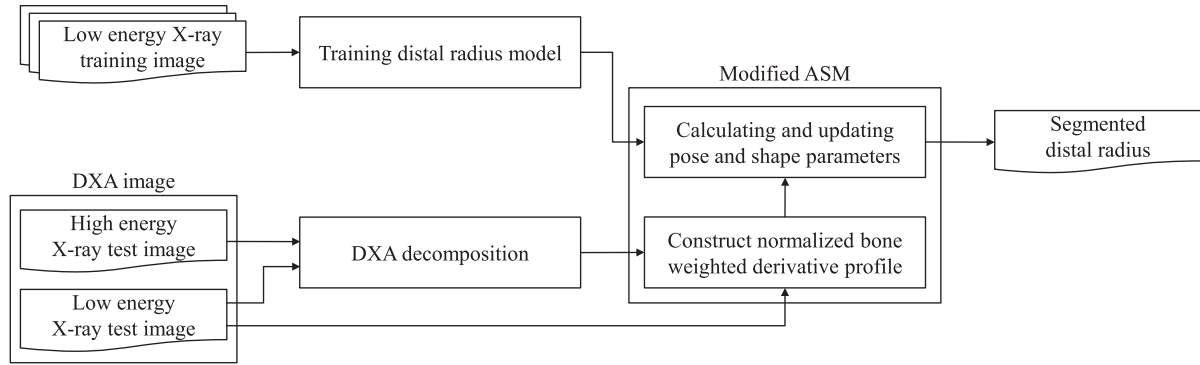


Fig. 3 Overview of the proposed distal radius segmentation method.

decomposition, and modified ASM. Using low energy X-ray training images, the training distal radius model analyzes the statistical shape distribution of the distal radius and the distribution of the edge strength around the boundary of the distal radius. The DXA decomposition module produces the DXA decomposed bone image, allowing emphasizing the bone region. To eliminate segmentation errors caused by the presence of a soft tissue edge, the modified version of ASM puts weights on the bone edge through the normalized bone weighted derivative profile (see Sect. 3.3 for more information about profiles). The modified version of ASM iteratively calculates and updates the pose and shape parameters to match the shape model of the distal radius and the boundary of the distal radius. The different modules and the enhanced version of ASM are explained in more detail in the following sections.

3.1 Training Distal Radius Model

The training distal radius model analyzes the statistical shape distribution of the distal radius and the distribution of the edge strength around the boundary of the distal radius using a set of labeled training images. The statistical shape distribution for the distal radius is modeled by making use of PDM [10]. To construct the shape distribution model, the distal radius is modeled using Low energy X-ray training images that have been manually annotated by a set of n points, representing different shapes. Let \mathbf{p}^u be a $2n$ element vector describing the n landmarks of the u -th distal radius in the training set: $\mathbf{p}^u = (x_1^u, y_1^u, x_2^u, y_2^u, \dots, x_n^u, y_n^u)^\top$. To construct the statistical shape model, it is necessary to compare equivalent points in the set of training images. All shapes in the training images are aligned using Procrustes analysis. Procrustes analysis was adopted in [11] to calculate rotation, scale, and translation parameters that minimize the distance between the corresponding landmarks.

After the alignment, the mean shape $\bar{\mathbf{p}}$ and the covariance matrix \mathbf{S} are computed as follows

$$\bar{\mathbf{p}} = \frac{1}{l} \sum_{u=1}^l \mathbf{p}^u, \quad (1)$$

$$\mathbf{S} = \frac{1}{l} \sum_{u=1}^l (\mathbf{p}^u - \bar{\mathbf{p}})(\mathbf{p}^u - \bar{\mathbf{p}})^\top, \quad (2)$$

where l represents the number of images in the training set. The mean shape $\bar{\mathbf{p}}$ is used when initializing ASM, placing the landmarks of $\bar{\mathbf{p}}$ on the test image. The eigenvalues of \mathbf{S} reflect the variance of the shapes described by the corresponding eigenvectors. The eigenvectors allow modeling the variation, this is, the way in which the landmarks move together as the shape varies. A shape instance \mathbf{p} can be reconstructed by linearly combining the mean shape with a weighted scaling of the matrix of the k eigenvectors:

$$\mathbf{p} = \bar{\mathbf{p}} + \Phi \mathbf{b}, \quad (3)$$

where Φ is a matrix whose columns are the first k eigenvectors corresponding to the k largest eigenvalues $\lambda_1, \lambda_2, \lambda_k$ of the covariance matrix \mathbf{S} . \mathbf{b} is a vector of shape parameters, weighing the influence of each eigenvector.

The statistical distribution of the edge strength in the region around a landmark is also analyzed. For a given landmark j , the mean normalized derivative model profile \bar{m}_e^j represents the average distribution of the edge strength on a perpendicular line to the shape boundary at the landmark aligned over the distal radius in the training set. The perpendicular line is centered at landmark j with length q . The e -th element of the derivative model profile is calculated by subtracting the intensity at the $e-1$ -th point on the perpendicular line from the intensity at the $e+1$ -th point on the perpendicular line [12]. After normalizing the derivative model profile, the mean normalized derivative model profile is computed by averaging the normalized derivative model profiles of the training set as follows:

$$\bar{m}_e^j = \frac{1}{l} \sum_{u=1}^l m_e^{j,u}, \quad (4)$$

where \bar{m}_e^j is the e -th element of the mean normalized derivative model profile at landmark j , and $m_e^{j,u}$ is the e -th element of the normalized derivative model profile at landmark j for the u -th training image. We also compute the $q \times q$ covariance matrix \mathbf{W} , providing a statistical description of the profile.

3.2 DXA Decomposition

In the DXA decomposition process, we construct a bone-emphasized digital radiographic image from DXA images. A DXA imaging system creates two different X-ray images of the same object, using different energy levels. This makes it possible to effectively differentiate bone and soft tissue [13]. The two different X-ray images are defined as follows:

$$I^{LE} = I_0^{LE} \exp(-(\mu_{soft}^{LE} \cdot T_{soft} + \mu_{bone}^{LE} \cdot T_{bone})), \quad (5)$$

$$I^{HE} = I_0^{HE} \exp(-(\mu_{soft}^{HE} \cdot T_{soft} + \mu_{bone}^{HE} \cdot T_{bone})), \quad (6)$$

where I^{LE} and I^{HE} are originating from the low and high energy detector, respectively. I_0^{LE} denotes the low energy emitted from the source, and I_0^{HE} denotes the high energy emitted from the source. μ_{soft}^{LE} and μ_{bone}^{LE} are the attenuation coefficients of the low energy for soft tissue and bone, respectively. Similarity, μ_{soft}^{HE} and μ_{bone}^{HE} are the attenuation coefficients of the high energy for soft tissue and bone, respectively. The four attenuation coefficient values can be found in [14]. T_{soft} denotes the thickness of soft tissue, and T_{bone} represents the thickness of bone. The following equation for DXA decomposition is proposed by [15]:

$$I_D = \exp(\log I^{HE} - w \cdot \log I^{LE}), \quad (7)$$

where I_D is the decomposed image, and w is a decomposition parameter. Using Eq. (5) and Eq. (6), Eq. (7) can be rewritten as follows:

$$I_D = \exp(\log I_0^{HE} - w \cdot \log I_0^{LE}) \cdot \exp((w \cdot \mu_{bone}^{LE} - \mu_{bone}^{HE}) \cdot T_{bone}) \cdot \exp((w \cdot \mu_{soft}^{LE} - \mu_{soft}^{HE}) \cdot T_{soft}). \quad (8)$$

In Eq. (8), it is possible to eliminate the soft tissue effect by adjusting the decomposition parameter w . The effect caused by the thickness of soft tissue T_{soft} can be ignored when $w \cdot \mu_{soft}^{LE} - \mu_{soft}^{HE} = 0$. In that case, the image only represents the effect from the bone. The bone-emphasized image, further referred to as DXA decomposed bone image I_D^{bone} , can be described as follows:

$$I_D^{bone} = \exp(\log I_0^{HE} - w \cdot \log I_0^{LE}) \cdot \exp((w \cdot \mu_{bone}^{LE} - \mu_{bone}^{HE}) \cdot T_{bone}). \quad (9)$$

3.3 Modified ASM

ASM iteratively tries to fit a shape model to the contour of the distal radius in a test image by adjusting pose and shape parameters. ASM starts by placing the landmarks of the mean shape $\bar{\mathbf{p}}$ of the distal radius on the test image. The test image is then sampled at each landmark, resulting in a set of model points. Each iteration matches the normalized derivative profile at model point i to the mean normalized

derivative model profile at the corresponding landmark. The magnitude of displacement for each model point is proportional to the distance from the model point to the point that fits best along the normal to the model boundary. The pose and shape parameters are calculated and updated by taking the displacement into account. When no significant change has been made to the shape in a previous iteration, the iterative process terminates.

To avoid segmentation errors caused by the presence of multiple edges in the near vicinity of the distal radius, the normalized derivative profile is weighted by the DXA decomposed bone image. Given model point i , the normalized bone weighted derivative profile h_i examines the statistics of the edge strength of the pixels in the vicinity of the model point. The pixels are typically normal to the model boundary centered at model point i with length r . The bone weighted derivative profile h_i^c represents the weighted profile before normalization. The c -th element of the bone weighted derivative profile is calculated as follows:

$$h_i^c = (I^{LE}(\mathbf{y}_i^{c+1}) - I^{LE}(\mathbf{y}_i^{c-1})) \times \alpha (I_D^{bone}(\mathbf{y}_i^{c+1}) - I_D^{bone}(\mathbf{y}_i^{c-1})), \quad (10)$$

where \mathbf{y}_i^c represents the coordinate of the c -th point along the normal to the boundary of model point i , and $I^{LE}(\mathbf{y}_i^c)$ and $I_D^{bone}(\mathbf{y}_i^c)$ are the gray level intensity in the low energy X-ray image and the DXA decomposed bone image at point \mathbf{y}_i^c , respectively. α is a weighting parameter for the DXA decomposed bone image. We then normalize the bone weighted derivative profile as follows:

$$h_i^c = \frac{h_i^c}{\sum_{a=1}^r |h_i^a|}, \quad (11)$$

where h_i^c represents the c -th element of the normalized bone weighted profile. This normalization makes the profile more invariant to changes in lighting [12]. The magnitude of displacements is determined by the distance between the model point and a point on the normal to the model boundary, minimizing the distance of the mean normalized derivative model profile at the corresponding landmark and the normalized bone weighted derivative profile at the model point. The magnitude of displacement can be represented as follows:

$$|d\mathbf{X}_i| = \|\arg \min_{\mathbf{v}_i} (f(\mathbf{g}_i^{\mathbf{v}_i}, \bar{\mathbf{m}}_j)), \mathbf{X}_i\|, \quad (12)$$

where $\|\cdot\|$ represents the Euclidean distance between two points, and \mathbf{X}_i is the coordinate of model point i . \mathbf{v}_i is the pixel coordinate along the normal to the boundary of model point i , and $\mathbf{g}_i^{\mathbf{v}_i}$ is the sub-interval of \mathbf{h}_i of length q pixels and centered at \mathbf{v}_i . The length of $\mathbf{g}_i^{\mathbf{v}_i}$ is shorter than the length of \mathbf{h}_i . $\bar{\mathbf{m}}_j$ is the mean normalized derivative model profile at landmark j corresponding to model point i . $f(\cdot)$ measures the Mahalanobis distance between the two profiles:

$$f(\mathbf{g}_i^{\mathbf{v}_i}, \bar{\mathbf{m}}_j) = \sqrt{(\mathbf{g}_i^{\mathbf{v}_i} - \bar{\mathbf{m}}_j)^T \mathbf{W}^{-1} (\mathbf{g}_i^{\mathbf{v}_i} - \bar{\mathbf{m}}_j)}, \quad (13)$$

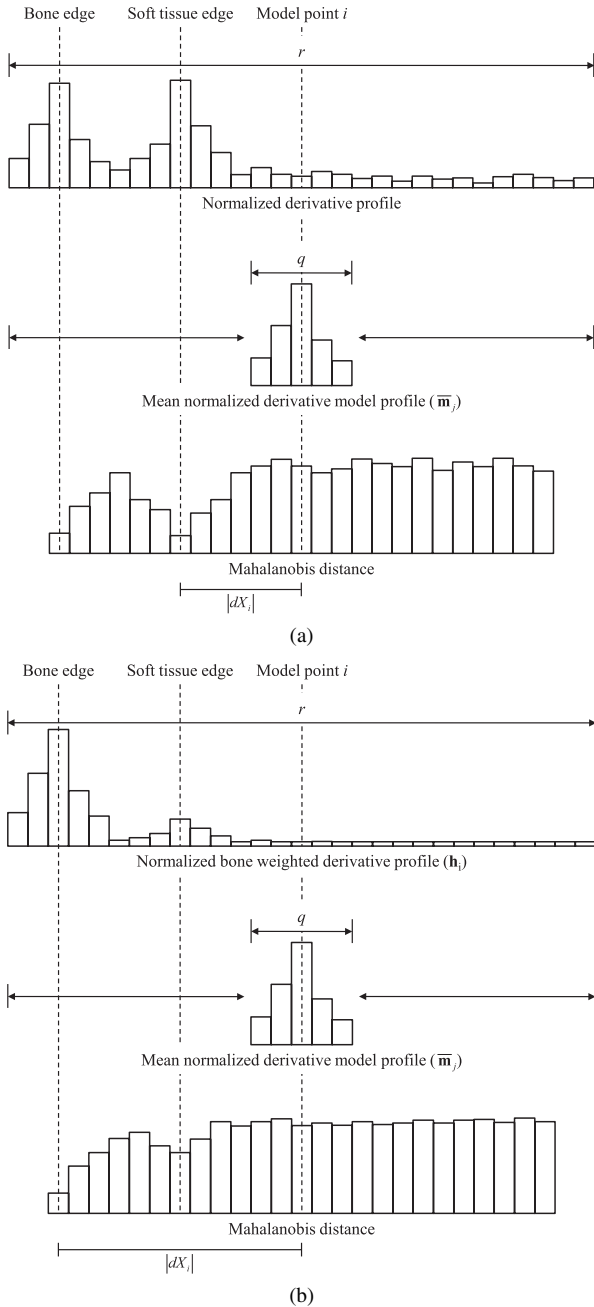


Fig. 4 Comparison of two methods for computing the magnitude of displacement at model point i ($|d\mathbf{X}_i|$): (a) magnitude of displacement computed with ASM; (b) magnitude of displacement computed with the proposed method.

where \mathbf{W} is the $q \times q$ covariance matrix for the normalized derivative model profile, computed by the training distal radius model process described in Sect. 3.1.

Figure 4 illustrates how the proposed normalized bone weighted derivative profile accurately calculates the magnitude of displacement at model point i by comparing the normalized derivative profile generally adopted in ASM. From Fig. 4(a), it can be easily observed that the magnitude of displacement is underestimated for the soft tissue edge. Because the hill at the soft tissue edge is often higher than the

hill at the bone edge, the Mahalanobis distance can be minimized at the soft tissue edge. The bone edge (the location to which the model point should be moved) cannot be easily differentiated from the soft tissue edge through fitting the mean normalized derivative model profile to the normalized derivative profile. As such, the magnitude of displacement for the model point is not suitable, resulting in segmentation errors.

As illustrated in Fig.4 (b), the normalized bone weighted derivative profile proposed in this paper effectively reduces the soft tissue effect and stresses the bone edge effect in the profile. The Mahalanobis distance is minimized at the bone edge because of the use of the proposed normalized bone weighted profile. By comparing Fig. 4 (a) with Fig. 4 (b), it can be seen that the normalized bone weighted derivative profile is able to correctly estimate the magnitude of displacement for model point i , thus avoiding segmentation errors when multiple edges are present.

When the displacements for the model points have been computed, denoted as a vector $d\mathbf{X} = (dx_1, dy_1, dx_2, dy_2, \dots, dx_n, dy_n)^T$, the displacements are compared to the image and a new set of displacements may be necessary. Given that the position of the model at each iteration is \mathbf{X} , the adjusted position is defined as $\mathbf{X} + d\mathbf{X}$. To find the best approximation of \mathbf{X} to $\mathbf{X} + d\mathbf{X}$, pose parameters (this is, rotation, scaling, and translation) are applied to the current state using a least square approach [11]. After applying pose parameters, residual displacements may be required, forcing the model point to be moved independently. As described in [10], the residual displacement $d\mathbf{X}$ is achieved by updating the shape parameter \mathbf{b} . To satisfy the constraint on \mathbf{b} , the updated shape parameter $d\mathbf{b}$ is approximated as follows:

$$d\mathbf{b} = \Phi^T d\mathbf{X}. \tag{14}$$

Let b_d represent the d -th element of the shape parameter \mathbf{b} , then the constraint is typically defined as $-3\sqrt{\lambda_d} \leq b_d \leq 3\sqrt{\lambda_d}$ [11]. λ_d , $1 \leq d \leq k$, is the corresponding eigenvalue from PDM. λ_d and Φ are described in Sect. 3.1. Algorithm 1 summarizes the proposed distal radius segmentation method using DXA images.

4. Experiments

4.1 DXA Image Acquisition

To verify the effectiveness of the proposed segmentation method, experiments were performed on 30 DXA images of the distal radius from 30 patients. Each DXA image consists of a high energy X-ray image and a low energy X-ray image, obtained from a cone beam DXA system that used 83 keV, 0.2 mA, and 1.5 sec as settings for creating the high energy X-ray image and that used 50 keV, 0.2 mA, and 1 sec as settings for creating the low energy X-ray image. The images have a pixel depth of 16 bits and the image resolution is 0.2 mm/pixel.

Algorithm 1. Proposed distal radius segmentation method

Training the distal radius model

- Every distal radius in the set of training images is manually annotated with 45 landmarks.
- Align the distal radius in the set of training images using Procrustes analysis.
- PDM is created for landmarks.
- The mean normalized derivative model profile $\bar{\mathbf{m}}$ at each landmark is computed.
- The covariance matrix \mathbf{W} is computed.

Segmenting the distal radius

- Construct DXA decomposed bone image I_D^{bone} from low and high energy X-ray test images.
 - An initial solution is estimated using the mean shape $\bar{\mathbf{p}}$.
 - Repeat
 - Construct the normalized bone weighted derivative profile h at each model point.
 - Find a point that minimizes the Mahalanobis distance between $\bar{\mathbf{m}}$ and the sub-interval of h centered at the point.
 - Calculate the displacement for each model point.
 - Calculate and update the pose and shape parameters under the constraint.
 - Until convergence
-

4.2 Experimental Results

The accuracy of the proposed segmentation method is characterized by calculating the point-to-line distance error for each point on the manually annotated distal radius contour. The sum of the Euclidean distance between each point in the manually annotated contour and the closest point in the segmented contour is divided by the number of points in the manually annotated contour. Figure 5 shows the point-to-line error for the 30 test images for two segmentation methods. In this paper, the value of α was determined as 1.2 using an empirical approach. Investigating the results achieved by the different segmentation approaches, it is clear that the proposed technique is able to guarantee a more accurate segmentation of the distal radius than ASM. The mean error of the proposed method is 0.512 mm with a standard deviation of 0.119 mm, and the mean error of ASM-based segmentation is 0.974 mm with a standard deviation of 0.275 mm. The proposed method is able to decrease the average point-to-line error by 47.4% compared to ASM-based segmentation.

Figure 6 illustrates the segmentation result for a test image using the two different segmentation methods outlined in this paper. The dashed box regions in Fig. 6 have been magnified to better show the difference between the obtained segmentation results. In the magnified image, the dashed line represents the manually annotated distal radius contour, and the segmentation results are represented with solid lines. Figure 6(a) shows the segmentation result for the conventional ASM method. A segmentation error can be observed in the distal radius region because the edge between the soft tissue and the background region is mistaken

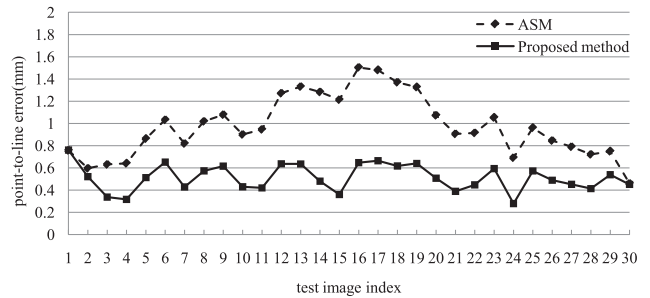


Fig. 5 Accuracy of distal radius segmentation in terms of point-to-line error.

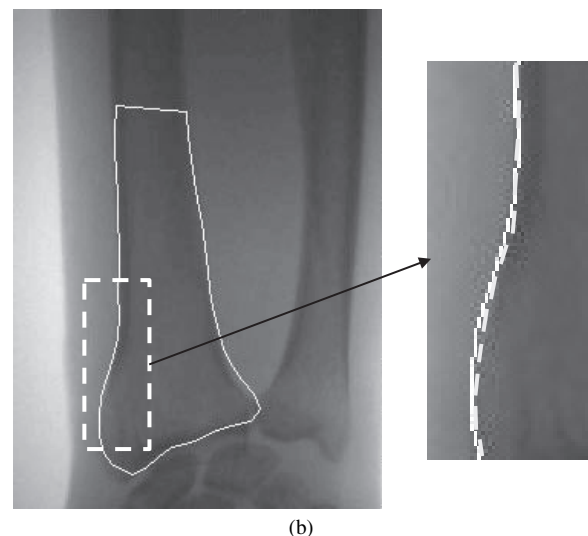
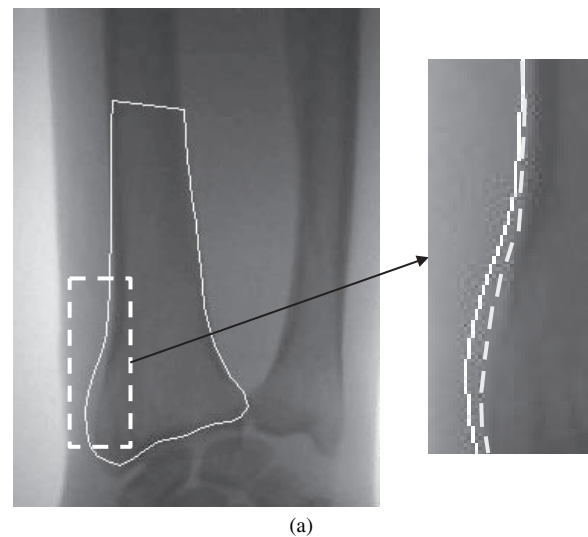


Fig. 6 Distal radius segmentation: (a) segmentation with ASM; (b) segmentation with the proposed method.

for the target edge. Figure 6(b) shows the segmentation result for the proposed segmentation method. As shown by the segmented contour, the distal radius area is more accurate than the distal radius area shown in Fig. 6(a).

As described in Eq. (10), the proposed normalized bone

Table 1 Segmentation performance according to α .

α	Average of point-to-line error	Variance of point-to-line error
0.2	0.718	0.144
0.4	0.654	0.131
0.6	0.597	0.119
0.8	0.580	0.116
1.0	0.529	0.106
1.2	0.512	0.102
1.4	0.525	0.105
1.6	0.551	0.108
1.8	0.542	0.110
2.0	0.567	0.113

weighted derivative profile varies according to the weighting value α . Table 1 shows the average point-to-line error and variance over the test images for different weighting values α . As shown in Table 1, the average point-to-line error and variance of the error are maximized when the weighting value α is set to 0.2. Further, the segmentation error decreases as the weighting value α becomes closer to 1.2.

5. Conclusion

BMD measurement using DXA, which has been attracting the interest of a lot of doctors, has come to be regarded as an essential criterion for evaluating a patient's risk of osteoporotic fracture. In this paper, we proposed an enhanced distal radius segmentation system: it guarantees accurate segmentation by taking advantage of DXA decomposed images, emphasizing bone edges by eliminating soft tissue. To verify the effectiveness of the proposed segmentation method, experimental results in terms of point-to-line distance error were presented. Our experimental results show that the proposed method accurately segments the distal radius. Further research on bone segmentation using DXA decomposition in proximal femur and spine, which are other major fracture sites, will be pursued.

Acknowledgment

This paper is supported by the development of MEXA image enhancement and processing (A080782) of Ministry for Health, Welfare and Family Affairs in Republic of Korea.

References

- [1] Conference report, "Consensus development conference: Diagnosis, prophylaxis, and treatment of osteoporosis," *American J. Medicine*, vol.94, pp.646–650, 1993.
- [2] J.E. Iglesias and M. Bruijne, "Semiautomatic segmentation of vertebrae in lateral X-rays using a conditional shape model," *Academic Radiology*, vol.14, no.10, pp.1156–1165, 2007.
- [3] J.E. Adams, "Single and dual energy X-ray absorptiometry," *European Radiology*, vol.7, no.10, pp.20–31, 1997.
- [4] V. Rebuffel and J.M. Dinten, "Dual-energy X-ray imaging: Benefits and limits," *Insight*, vol.49, no.10, pp.589–594, 2007.
- [5] M. Seise, S.J. McKenna, I.W. Ricketts, and C.A. Wigderowitz, "Learning active shape models for bifurcating contours," *IEEE Trans. Med. Imaging*, vol.26, no.5, pp.666–677, 2007.

- [6] G. Zamora, H. Sari-Sarraf, and R. Long, "Hierarchical segmentation of vertebrae from X-ray images," *Proc. SPIE Medical Imaging*, vol.5032, pp.631–642, 2003.
- [7] J.M. Sotoca, J.M. Inesta, and M.A. Belmonte, "Hand bone segmentation in radioabsorptiometry images for computerised bone mass assessment," *Computerized Medical Imaging and Graphics*, vol.27, no.6, pp.459–467, 2003.
- [8] S. Hagiwara, K. Engelke, M. Takada, S.O. Yang, S. Grampp, M.S. Dhillon, and H.K. Genant, "Accuracy and diagnostic sensitivity of radiographic absorptiometry of the second metacarpal," *Calcified Tissue International*, vol.62, no.2, pp.95–98, 1998.
- [9] H.W. Wahner, B.L. Riggs, and J.W. Beabout, "Diagnosis of osteoporosis: Usefulness of photon absorptiometry at the radius," *J. Nuclear Medicine*, vol.18, no.5, pp.432–437, 1977.
- [10] T.F. Cootes, C.J. Taylor, D. Cooper, and J. Graham, "Active shape models-their training and application," *Computer Vision and Image Understanding*, vol.61, no.1, pp.38–59, 1995.
- [11] T.F. Cootes, C.J. Taylor, D. Cooper, and J. Graham, "Training models of shape from sets of examples," *Proc. British Machine Vision Conference*, pp.9–18, 1992.
- [12] T.F. Cootes, C.J. Taylor, D. Cooper, and J. Graham, "Building and using flexible models incorporating grey-level information," *Proc. International Conference on Computer Vision*, pp.242–246, 1993.
- [13] A. Pietrobelli, C. Formica, Z. Wang, and S.B. Heymsfield, "Dual-energy X-ray absorptiometry body composition model: Review of physical concepts," *American J. Physiology*, vol.271, pp.941–951, 1996.
- [14] J.H. Hubbell and S.M. Seltzer, "Tables of X-ray mass attenuation coefficients and mass energy-absorption coefficients," <http://physics.nist.gov/PhysRefData/XrayMassCoef/tab4.html>, 1996.
- [15] J.W. Kwon, S. Cho, Y.B. Ahn, and Y.M. Ro, "Bone region extraction by dual energy absorptiometry image decomposition," *Journal of Korea Multimedia Society*, vol.12, no.9, pp.1233–1241, 2001.



Sihyoung Lee received the B.S. degree from Kyunghee University, South Korea, in 2005, and the M.S. degree from the Information and Communications University, South Korea, in 2007. At present, he is a Ph.D. candidate at the Korea Advanced Institute of Science and Technology. His research interests include medical image segmentation, content-based image analysis, and image annotation.



Sunil Cho received the B.S. degree in Electrical Engineering from the Information and Communications University, South Korea, in 2006, and M.S. degree from the Korea Advanced Institute of Science and Technology, South Korea in 2010. He now works for Agency for Defense Development in South Korea. His research interests include object segmentation, mammography, and noise reduction.



Yong Man Ro received the B.S. degree from Yonsei University, Seoul, Korea, and the M.S. and Ph.D. degrees from the Korea Advanced Institute in Science and Technology, South Korea. In 1987, he was a Researcher with Columbia University, New York, NY, and from 1992 to 1995, he was a Visiting Researcher with the University of California, Irvine, and with KAIST. In 1996, he was a Research Fellow with the University of California, Berkeley. He is currently a Professor and the Director of the Im-

age and Video System Laboratory, Korea Advanced Institute of Science and Technology, South Korea. He participated in international standardizations including MPEG-7 and MPEG-21, where he contributed several MPEG-7 and MPEG-21 standardization works, including the MPEG-7 texture descriptor and MPEG-21 DIA visual impairment descriptors and modality conversion. His research interests include image/video processing, multimedia adaptation, visual data mining, image/video indexing, and multimedia security. Dr. Ro was the recipient of the Young Investigator Finalist Award of the International Society for Magnetic Resonance in Medicine in 1992 and the Scientist Award (Korea), in 2003. He has served as a Technical Program Committee member for many international conferences, including the International Workshop on Digital Watermarking (IWDW), Workshop on Image Analysis for Multimedia Interactive Services (WIAMI), Asia Information Retrieval Symposium (AIRS), Consumer Communications and Networking Conference, etc., and as the Co-Program Chair of the 2004 IWDW.